Laser-Induced Graphene Formation on Chitosan Derivatives toward Ecofriendly Electronics

Huang, Qian Ming; Yang, Huiru; Wang, Shaogang; Liu, Xu; Tan, Chunjian; Luo, Anxin; Xu, Siyuan; Zhang, Guoqi; Ye, Huaiyu

DOI
10.1021/acsanm.3c01408

Publication date
2023

Document Version
Final published version

Published in
ACS Applied Nano Materials

ACS APPLIED NANO MATERIALS

www.acsanm.org

Article

Laser-Induced Graphene Formation on Chitosan Derivatives toward Ecofriendly Electronics

Qian-Ming Huang, Huiru Yang, Shaogang Wang, Xu Liu, Chunjian Tan, Anxin Luo, Siyuan Xu, Guoqi Zhang, and Huaiyu Ye*

Cite This: *ACS Appl. Nano Mater.* 2023, 6, 10453−10465

Read Online

ACCESS | Metrics & More | Article Recommendations | Supporting Information

ABSTRACT: Laser-induced graphene (LIG) has aroused a wide range of research interests ranging from micro-nano energy devices to the Internet of Things (IoT). Nevertheless, the non-degradability of most-used synthetic polymer carbon sources poses a serious threat to the environment. In this work, ecofriendly chitosan-based derivatives, including carboxymethyl chitosan (CMCS), chitosan oligosaccharide, and chitosan hydrochloride, are successfully converted into LIGs for the first time via a convenient one-step CO_2 laser engraving at ambient air. The obtained LIGs are characterized by a three-dimensional hierarchical porous structure and exhibit good sheet conductivity. The consecutive carbonization and graphitization mechanism of target precursors induced by laser heat accumulation is also deeply discussed. Besides, based on a mechanically reliable LIG/CMCS composite film and tribo-negative acrylic/polyimide anti-layers, two contact-separation mode triboelectric nanogenerators are built and their power densities range from 1.44 to 2.48 mW cm^{-2}. These devices with long cycle life can be used for low-frequency mechanical energy harvesting and commercial capacitance charging, which could be potentially applied in the wireless sensor network nodes. Such a family of chitosan derivatives paves a new route for LIG synthesis and provides new ideas for ecofriendly LIG electronics.

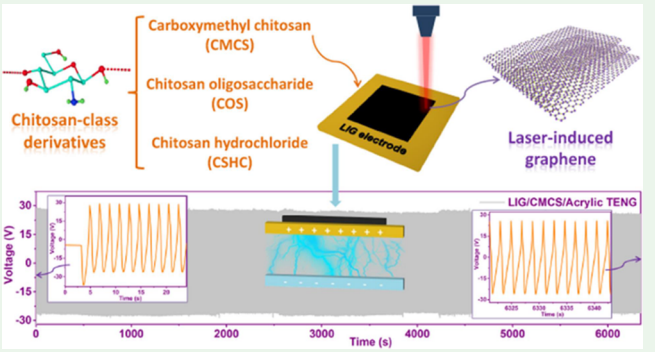

KEYWORDS: *laser-induced graphene, carbon precursor, chitosan derivatives, ecofriendly and biodegradability, triboelectric nanogenerator*

Three-dimensional (3D) hierarchically porous laser-induced graphene (LIG) has newly emerged as a hot-pot material in physical, chemical, and engineering fields due to its excellent electrical conductivity, large surface area, high porosity, and superior mechanical and thermal natures.[1−5] Based on the convenient direct laser-writing (DLW) method, patternable LIGs can be easily obtained on numerous carbon-rich polymer substrates with controllable surface micro-structure, electrical conductivity, and other physicochemical properties.[6−9] Compared with conventional synthesis and patterning routes such as lithography and chemical etching, DLW does not require any masks, toxic chemical reagents, or high energy consumption, which is highly favorable for the large-scale and cost-efficient preparation of the 3D graphene structure and corresponding microelectronic devices.[5,10−13] On account of the unique superiority of the DLW technology and outstanding performance of LIG, various advanced LIG applications, including triboelectric nanogenerators (TENGs), supercapacitors, batteries, sensors, etc., have been widely developed, giving a huge boost to carbon-based micro-nano electronics.[14−22]

Since the attractive LIG was first discovered on the polyimide (PI) by Tour's group,[23] the synthesis and functionalization of LIG have made great progress.[24−26] Generally, the starting materials should be the most critical factor in consideration for LIG electronics because they not only are the carbon source depending on the composition, microstructure, and property of obtained LIGs but also often serve as the mechanical support and functional component to assist corresponding micro-nano applications.[2,27,28] For example, the flexible PI substrate as both the LIG electrode attachment layer and tribo-material was assembled into TENG for energy harvesting and smart sensing.[29−31] Up to now, synthetic plastic polymers should be the most-used substrate materials due to their good electrical insulation, mechanical flexibility, chemical stability, etc.[32−37] Based on the synthetic plastics, it has also been revealed that the LIG formation mainly involves laser-induced photo-conversion reaction, and repeated aromatic groups within the polymer structure play a

Received: March 30, 2023
Accepted: May 18, 2023
Published: June 1, 2023

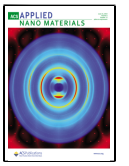

https://doi.org/10.1021/acsanm.3c01408
ACS Appl. Nano Mater. 2023, 6, 10453−10465

pivotal role.[23,38,39] However, the non-biodegradable property of plastic polymers poses a serious threat to the environment, and the resulting synthetic polymer-based LIG devices will exacerbate the rapid generation of electronic waste (e-waste).

Faced with the ever-increasing amount of e-waste, "green" carbon-based devices are highly desired. Hence, for the development of LIG electronics, it is of great significance to explore natural or biodegradable carbon precursors to help establish a more ecofriendly society. Renewable natural biomass materials afford great potential for this environmentally friendly goal. Based on this idea, LIG was first isolated from natural plant pinewood,[40] and subsequently, a series of lignin/cellulose-rich materials, including wood, paper, cloth, leaf, or even food, all demonstrated that they can be pyrolyzed into LIG.[40−45] Nevertheless, LIG formation from these natural carbon sources still faces many obstacles. A major challenge is that the lignin/cellulose component can be easily ablated or burned into versatile gases in ambient air due to their flammable nature, and special flame retardant treatment (such as reduced/inert gas atmospheres and fire retardants) or processing techniques (such as low-throughput multistep laser and short-pulsed femtosecond laser) have to be adopted,[42,46−48] which increases the preparation cost and process difficulty. In addition, the complex composition and irregular shape of natural products also bring out serious variations in LIG quality and properties in different batches, highly limiting the large-scale preparation of target products with good uniformity. For these reasons, the use of synthetic polymers in numerous LIG applications has not been effectively reduced to date. Therefore, developing ecofriendly carbon precursors remains a pivotal task and a big challenge for ecofriendly LIG electronics.

Chitosan (chitin) is a highly renewable natural polymer material, widely found in marine crustacean shells (shrimps and crabs, etc.) and second only to the cellulose on earth.[49−52] Current utilization domains of chitosan-based polymers (including chitosan and its synthetic derivatives) have involved textile, agriculture, environmental protection, beauty care, etc.[50,53] Similar to cellulose, chitosan-based polymers also take a hexagonal pyran ring as the core building unit (Figure S1), which provides an intrinsic structural fundament (repeated aliphatic units) for the possibility of LIG formation. Additionally, chitosan-class polymers are not easily ablated directly into volatile gases due to their excellent flame-retardant properties.[54,55] Furthermore, chitosan derivatives with good water solubility can be easily prepared into films with an extremely uniform composition similar to synthetic plastics, which is conducive to stable device preparation by the planar process. Therefore, chitosan and its derivatives are a class of potential carbon source precursors and may bring new opportunities for LIG preparation and application. Most recently, Lin and coworkers have employed a 5-axis laser processing platform to prepare LIG conformal electronics on chitosan-containing shells.[56] However, the growth of LIG on curved shells appears to be uneven and the transition from shell to LIG was not yet revealed in depth. In this work, our efforts in the chitosan polymer system have demonstrated that pre-prepared carboxymethyl chitosan (CMCS), chitosan oligosaccharide (COS), and chitosan hydrochloride (CSHC) films can be directly converted into LIG via convenient one-step CO_2 laser ablation in an ambient atmosphere. The basic physicochemical and surface properties of these obtained LIGs were also characterized. Besides, based on the mechanically reliable LIG/CMCS film, metal electrode-free TENG devices were constructed for low-frequency machine energy harvesting and ceramic capacitor charging. This work revealed a new class of biodegradable LIG precursors and demonstrated the potential micro-nano electronic application of fabricated LIG composites. Herein, we report the syntheses, characterizations, and TENG applications of the target LIGs.

RESULTS AND DISCUSSION

Chitosan is an important natural organic precursor molecule with many substitutable sites, and therefore, a good amount of derivatives with unique characteristics can be obtained from chitosan through oriented reactions.[49,50,52,53] In this study, three hydro-soluble derivatives (CMCS, COS, and CSHC, Figures 1a and S2) were selected as potential carbon sources

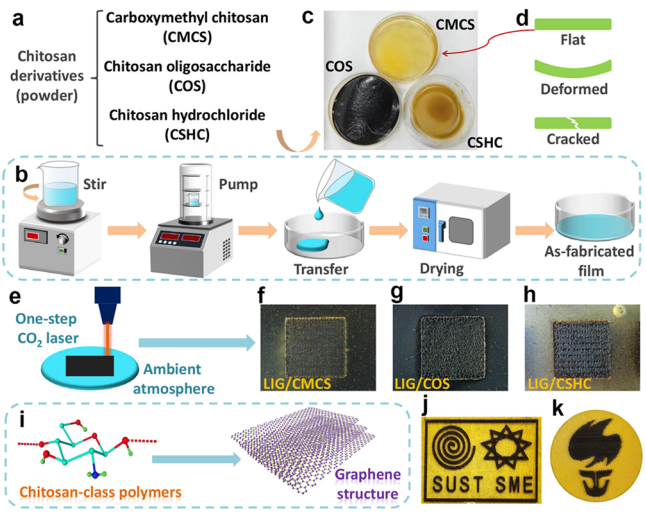

Figure 1. (a) Three utilized chitosan derivatives and their abbreviation. (b) Schematic of film fabrication of target polymers. (c) As-prepared CMCS, COS, and CSHC films placed in plastic dishes with a diameter of 66 mm. (d) Three cross-sectional types of the resulting films. (e) Schematic of one-step CO_2 laser reduction carbonization. Photographs of (f) LIG/CMCS, (g) LIG/COS, and (h) LIG/CSHC composite films with a 5.0 × 5.0 mm^2 LIG square. (i) Schematic of laser-induced structure evolution from chitosan derivatives to 3D porous graphene. (j, k) Pictures of LIG patterns on the CMCS film with arbitrarily designed shapes.

for LIG fabrication. These three as-received powder samples were fabricated into film substrates and then utilized to implement laser pyrolysis, and the schematic in Figure 1b concisely describes the whole process. As shown in Figure 1c,d, the flatter CMCS film seems the best candidate for the planar laser process and device fabrication compared with its other counterparts with deformed and cracked surfaces. CSHC and COS films have a certain degree of stress-induced deformation and obvious brittle fracture, which can be attributed to their weak plasticity and high sensitivity to stress variables such as temperature and humidity. Long-term observation also found that only CMCS film can maintain a high degree of mechanical reliability and stability even when placed in an indoor environment for several months. These as-prepared films were then engraved by a facile commercial 10.6 μm infra-red CO_2 laser under an ambient atmosphere (Figure 1e), and a more specific process is represented in the Experimental Section.

https://doi.org/10.1021/acsanm.3c01408
ACS Appl. Nano Mater. 2023, 6, 10453−10465

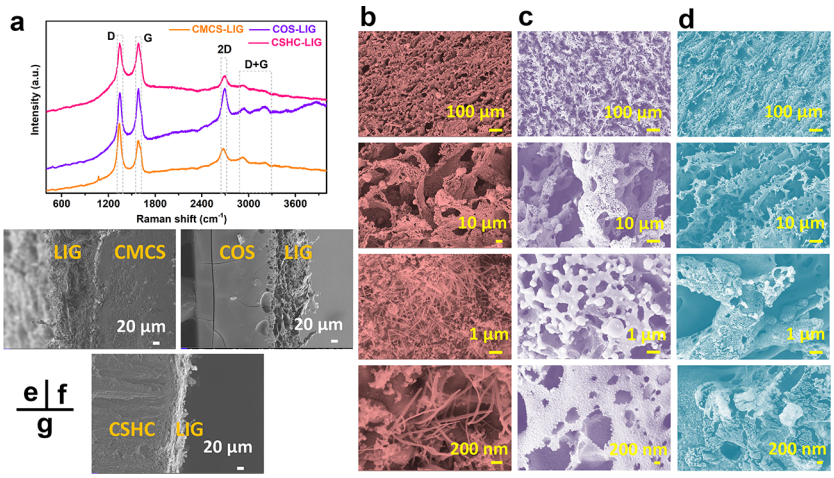

Figure 2. (a) Raman spectra of the resulting CMCS-LIG, COS-LIG, and CSHC-LIG samples. The SEM images of (b) CMCS-LIG, (c) COS-LIG, and (d) CSHC-LIG at four different resolutions (scale bars: 100 μm, 10 μm, 1 μm, and 200 nm). Cross-sectional images of (e) LIG/CMCS, (f) LIG/COS, and (g) LIG/CSHC composite films.

The preliminary results revealed that these three species all can be transformed into black and conductive LIG materials, and Figure 1i displays the relative schematic diagram of structure evolution from chitosan derivative molecule to LIG networks. Figure 1f–h exhibits the photographs of the as-fabricated CMCS-LIG, COS-LIG, and CSHC-LIG samples obtained under the laser powers of 4.8, 5.6, and 5.2% (the percentage is the duty cycle, and the rated power is 40 W), respectively, and the resistance test suggested that they are conductive squares, which will be systematically analyzed in the later section. As shown in Figure 1j,k, except for the strict square shape, the polymer substrates can also be easily patterned with arbitrary shapes based on the designed routes and the formed LIG conductive paths can be removed again by laser cutting or laser pyrolysis, which indicate the good editable property of engraved LIGs. Editable LIG circuits with electrically insulated substrates are compatible with the planar microelectronic process and could facilitate their application in carbon-based micro-nano devices. Several physical and chemical measurements were utilized to characterize these one-step synthesized LIGs.

The transformation from carbon precursor to a few-layer graphene structure was evidenced by the Raman spectra of both chitosan polymers and corresponding LIGs depicted in Figures 2a and S4. The G peaks (from 1582 to 1588 cm^{-1}, Table S1) along with the sharp 2D peaks (2665–2700 cm^{-1}) in Figure 2a reveal the characteristic bands of the graphene network.[57] These 2D band profiles are consistent with the graphite-carbon structures with randomly stacked graphene layers, thus confirming the formation of LIG.[58,59] At the same time, the obvious D (1341–1347 cm^{-1}) and D + G peaks propose that the porous LIG has an essential characteristic of defective states.[23] In addition, in terms of the crystalline quality of present objectives, CMCS-LIG indicates a relatively larger D/G peak intensity than COS-LIG and CSHC-LIG, and a larger I_{2D}/I_G ratio of COS-LIG means that it has better few-layer properties than CMCS-LIG and CSHC-LIG (Figure S5). Notably, different experiment conditions will greatly affect the quality and properties of resulting LIG products, which has been widely demonstrated in both synthetic and natural polymer systems.[60,61]

The microscopic morphologies of these three LIGs were studied by secondary-electron scanning electron microscopy (SEM) at different resolutions (Figure 2b–d). Under the resolutions of 100 and 10 μm, it can be seen that they share a similar porous structure with a mixture of strip-like and sheet-like components, which is somewhat similar to the appearance of coral reefs. However, CMCS-LIG and CSHC-LIG appear to be more densified than COS-LIG because the latter presents coarser strip units and larger porosity. Additionally, these LIG structures all exhibit relatively rough edges, which could be attributed to the ambient experimental circumstance and excess oxidation of graphene structure.[60] Their finer and more microscopic images were further revealed at resolutions of 10 μm and 200 nm. CMCS-LIG is characterized by micron-sized fiber where large amounts of aggregated carbon nanoparticles are attached to the surroundings, whereas COS-LIG displays spherical and porous sheet structures; as for CSHC-LIG, it still features strip-like structures composed of snowflake subunits. It has been proved that fibrous LIG has a large number of defects, and the aggregated carbon clusters could be formed in a lased-induced high-pressure environment.[62] Cross-sectional diagrams (Figure 2e–g) of these LIGs indicate that their thicknesses are around 50–100 μm, and CMCS-LIG and CSHC-LIG layers are denser, while COS-LIG has a more porous structure. Moreover, the cracks inside the COS film can also be observed (Figure 2f), which is consistent with the previous description. Transmission electron microscopy (TEM) measurements were also performed to deeply realize their microscopic morphologies at the nanoscale, and ribbon or sheet-shaped graphene structures were observed under resolutions of 50 and 20 nm (Figure S6). Zoomed-in TEM images further reveal the ripple-like wrinkled edges of the light and thin LIG layers, which could be ascribed to the thermal expansion during high-energy CO_2 laser irradiation.[23] It can be observed that CMCS-LIG and COS-LIG show relatively dense stripes compared to CSHC-LIG with a thinner layering. Moreover, the characteristic d-spacing of ~0.34 nm can be measured from the edges of adjacent flakes, corresponding to the distance between (002) lattice planes of few-layer graphene.[23]

The surface chemistry of as-obtained LIGs with corresponding polymer substrates was also investigated by X-ray

https://doi.org/10.1021/acsanm.3c01408
ACS Appl. Nano Mater. 2023, 6, 10453–10465

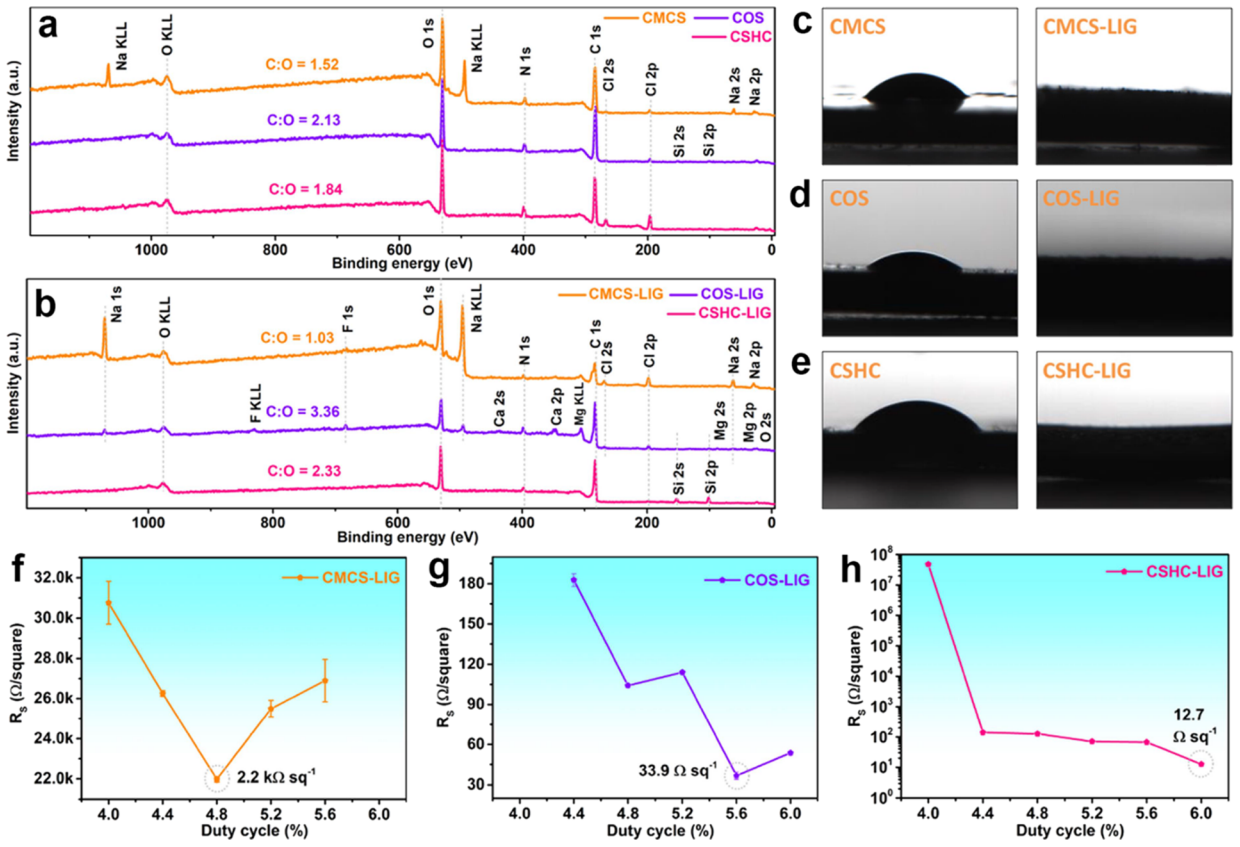

Figure 3. (a) Survey XPS spectra of CMCS, COS, and CSHC substrates, and (b) CMCS-LIG, COS-LIG, and CSHC-LIG films. The water droplet appearance on the surface of (c) CMCS & CMCS-LIG, (d) COS & COS-LIG, and (e) CSHC & CSHC-LIG, respectively. The water droplet appears to have a contact angle of 0° at all three LIG surfaces. The sheet resistance (R_S) of square (f) CMCS-LIGs, (g) COS-LIGs, and (h) CSHC-LIGs obtained at various laser powers ranging from 4.0 to 6.0% with a step of 0.4% (rated power: 40 W).

photoelectron spectroscopy (XPS) characterization. The survey scan spectra in Figure 3a,b indicate the elemental distribution and content change trend from precursors to LIGs. For LIGs, the presence of non-metallic C, O, N, Cl, and metallic Na (CMCS-LIG) could come from themselves or unconverted substrates, or even be introduced from the synthesis environment (O from the air), while other slight elements, such as Si, F, Ca, and Mg should be impurities or pollutants that originate from laser reaction and measurement processes. A more specific percentage of content information is counted in Table S2. The C/O atomic ratio of COS-LIG and CSHC-LIG is significantly higher than that of their parent compounds, confirming the loss of O atoms and the successful carbonization and graphitization of carbon sources after DLW treatment. Interestingly, CMCS-LIG discloses a conversely lower C/O ratio than CMCS, which means that the laser processing of CMCS in the air leads to relatively weak carbonization and graphitization and the corresponding LIG contains a large number of oxygen-containing groups. Additionally, unlike non-metallic C and N elements that can be released as gases such as CO and N_2, metallic Na elements as main impurities remain in the final products, and the percentage is also increased. Given the high solubility of these ions and anions, the compositions of the as-prepared films are highly stable and can be measured. High-resolution C1s and N1s spectra of LIGs were further deconvoluted into more specific peaks to reveal diversified functional groups. The deconvoluted high-resolution C1s (Figure S7a−c) spectra could be fitted into C−C/C═C, C−N, C−O/C−O−C, N−C═O/O−C−O, O−C═O, $\pi-\pi^*$, etc. It can be noticed that, except for the prominent C−C/C═C peaks, the oxygen-containing groups are very abundant and occupy a considerable proportion, which could originate from the oxidized LIGs or unconverted precursors. In addition, the oxygen element content of the CMCS-LIG is relatively higher than those of COS-LIG and CSHC-LIG, following its high defect-state content. Furthermore, the C−N is present in all three LIGs, which can be ascribed to the unconverted polymer components. Additionally, noteworthy is that CSHC-LIG presents an almost negligible $\pi-\pi^*$ satellite peak, signifying its fewer-layer structure compared to CMCS-LIG and COS-LIG. These LIGs have relatively high nitrogen content and the high-resolution N1s spectra disclose (Figure S7d−f) that, for each sample, the pyridinic-N is the dominant component, as well as a small amount of pyrrolic-N, while the quaternary-N is almost negligible. These XPS analyses are very similar to that of cellulose paper-based LIG.[46]

In comparison with a pure graphene structure, 3D porous LIG with self-doped O and N elements often possesses more unique chemical and physical natures, such as enhanced hydrophilicity.[63] Thus, the surface contact property of these LIGs with water was also measured (Figure 3c−e). It can be observed that the original contact angles for CMCS, COS, and CSHC films are 48.42, 38.78, and 50.91°, respectively, indicating their strong hydrophilic capacity. When the raw materials are transformed into LIGs, the contact angles are dramatically declined to 0°, unveiling remarkable super-hydrophilic properties. The laser-induced graphitization leads

https://doi.org/10.1021/acsanm.3c01408
ACS Appl. Nano Mater. 2023, 6, 10453−10465

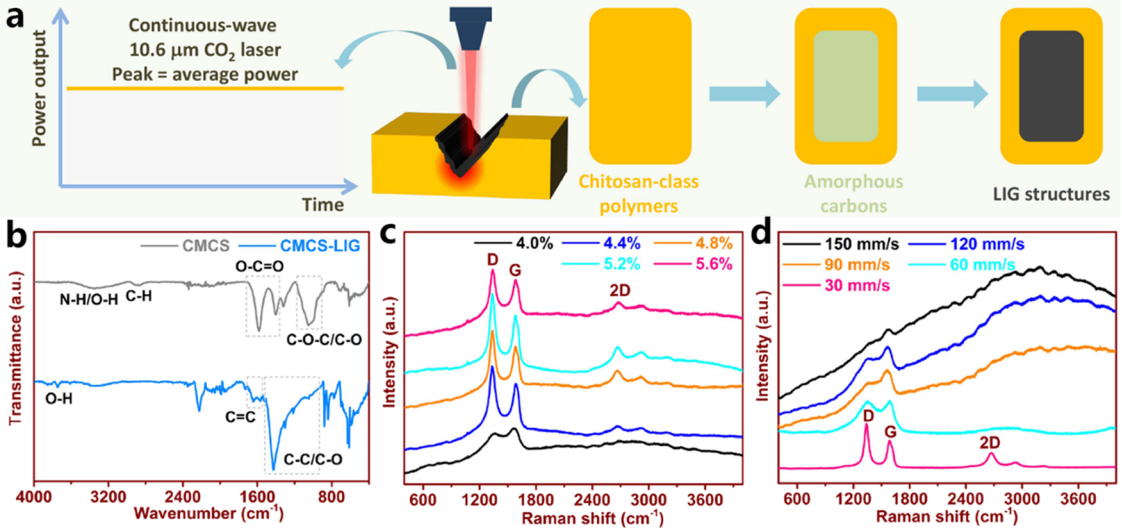

Figure 4. (a) Schematic illustration of the mechanism of LIG formation from chitosan-class polymers. (b) FTIR spectra of CMCS and CMCS-LIG. Raman spectra of CMCS-LIGs obtained at (c) different laser powers with a DLW speed of 30 mm/s and (d) recorded at different DLW speeds with a laser power of 5.2%.

to an apparent transformation from hydrophilicity to super-hydrophilicity in chitosan polymer substrate interfaces. Their super-hydrophilic ability should be ascribed to both good chemical and physical adsorption abilities. On the one hand, abundant O and N elements greatly facilitate the interaction between water and surface due to the highly polar C−O/C═O bonds and nitrogen-containing hydrophilic active sites;[40,63] on the other hand, the porous sheet-like microstructures (Figure 2b−d) with low roughness is proved to be beneficial to the surface physical adsorption of LIGs because of the collapse and impregnation of water droplets at the interface.[60,64,65] These interface properties could facilitate their potential applications in supercapacitor and water−oil separation, etc.[5]

Although different applications often require customized LIGs with unique properties, low resistivity is applicable in many situations to achieve high-quality micro-nano electronic devices. Regulating the laser power while controlling for other variables allows rapid access to the laser processing conditions for low-resistance LIG.[24] Here, based on the one-step laser engraving, the effect of laser power on sheet resistance was systematically evaluated. The precursor films were ablated under laser powers from 4.0 to 6.0% with a step of 0.4%, and the DLW speed and pixel step was set as 30 mm/s and 2, respectively. As illustrated in Figures S8−S10, these lased samples are carbonized within the defined power ranges, but with the enhancement of the laser power, the charred squares will be gradually damaged or even crumbled attributing to excessive energy input. Hence, the threshold laser powers are 5.6, 6.0, and 5.6% for CMCS, COS, and CSHC, respectively. The sheet resistance of these black squares was also measured to roughly assess their crystalline quality and electrical performance, and the results propose that most of them are electrically conductive, except for some samples treated at too small or too large powers (Figure 3f−h). The former can be attributed to the inability to achieve graphitization at lower laser power, while the latter should result from severe damage to the samples. Overall, within the threshold power, the sheet resistance gradually decreases with the enhancement of laser powers for each set of samples. The minimum sheet resistance of CMCS-LIG, COS-LIG, and CSHC-LIG is 2.2 kΩ sq^{-1}, 33.9 Ω sq^{-1}, and 12.7 Ω sq^{-1}, respectively, under the corresponding laser power of 4.8, 5.6, and 6.0%. The optimal sheet resistance of COS-LIG and CSHC-LIG is comparable to most of LIGs prepared by synthetic plastic or lignocellulose-based precursors (Table S3), such as PI-LIG (15 Ω sq^{-1}) and wood-LIG (10 Ω sq^{-1}),[23,40] which demonstrates that chitosan derivatives based LIGs possess good electrical properties, and chitosan-class polymers are a promising family of carbon precursors for the development of biodegradable LIG electronics. By comparison, CMCS-LIG has a relatively high sheet resistance level compared to its counterparts due to a lower degree of graphitization and a highly defective crystalline structure.

The mechanism of LIG formation is related to the interaction between the incident laser and carbon-containing organic polymers. A cost-effective and facile commercial CO_2 laser with high energy conversion efficiency and high reliability is the ideal equipment for pyrolysis processing and LIG preparation. It has been reported that long wavelength continuous-wave (ultra-long pulse duration) infra-red CO_2 laser (Figure 4a) can realize the LIG conversion of almost all forms of known carbon sources under proper processing conditions whether they are synthetic or natural high-molecular polymers.[5,8,66] It has been generally recognized that localized high temperature and high pressure induced by the energy accumulations of CO_2 laser result in the break of various chemical bonds of polymer molecules, and the release of gaseous products and rearrangement of carbon atoms leads to the formation of intermediate amorphous carbon and final LIG networks during a very short transient time.[23,38] Therefore, the direct transformation of chitosan-class polymers to LIG is also expected based on laser heat accumulation-induced consecutive carbonization and graphitization (Figure 4a). The conversion of mechanically stable CMCS into LIG resulting from the intense photo-thermal effect was investigated in detail. As shown in Figure 4b, the Fourier-transform infrared (FTIR) spectrum of the CMCS displays its characteristic absorption bands at 3350 cm^{-1} (stretching vibration peak of O−H/N−H), 2866 cm^{-1} (stretching vibration peak of C−H), 1581 and 1400 cm^{-1} (stretching vibration peaks of O−C═O), and 1049 cm^{-1} (stretching vibration peak of C−O−

https://doi.org/10.1021/acsanm.3c01408
ACS Appl. Nano Mater. 2023, 6, 10453−10465

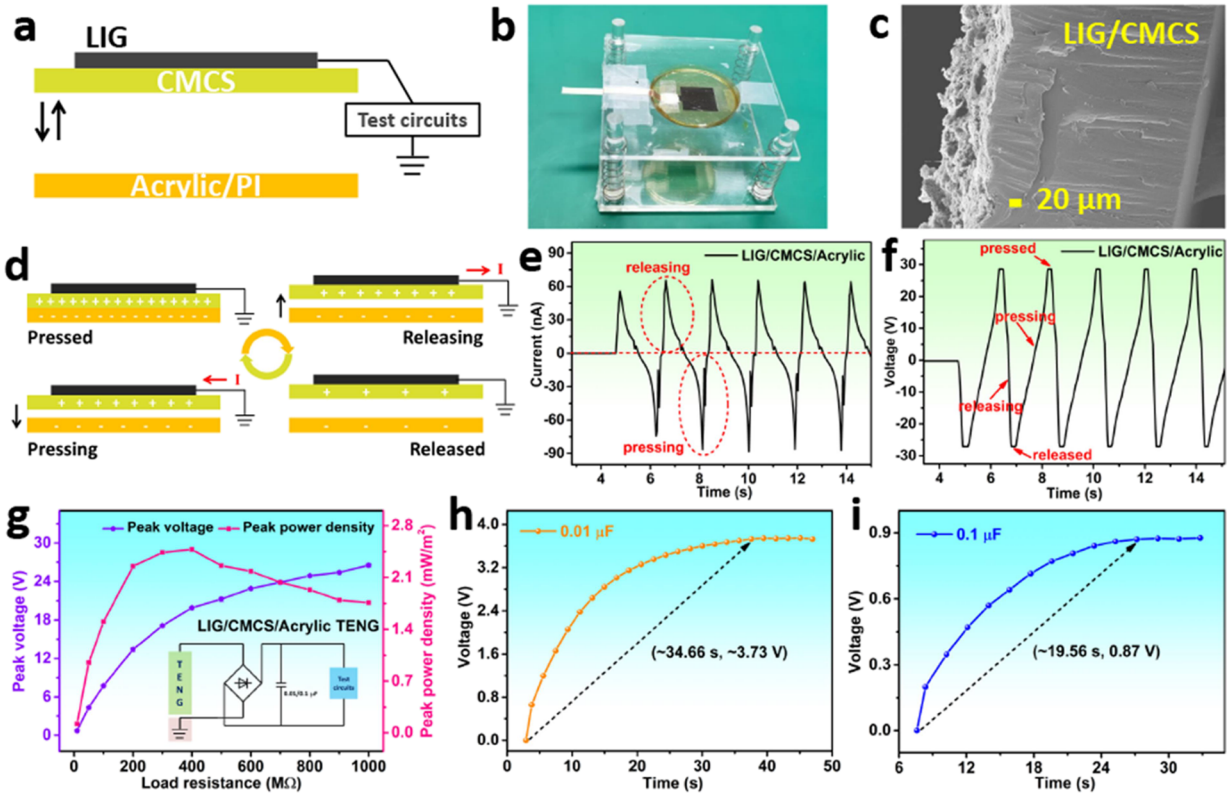

Figure 5. (a) Schematic of CS mode TENG, and (b) picture of real LIG/CMCS/Acrylic TENG device where the LIG/CMCS composite film with the 20 × 20 mm^2 LIG electrode is encapsulated by silver paste, copper wire, and tape. (c) Cross-sectional image of the new-fabricated LIG/CMCS composite film for TENG devices. (d) Mechanism for power generation of LIG/CMCS-based TENGs. (e) V_{OC} and (f) I_{SC} of LIG/CMCS/Acrylic TENG. (g) Peak voltage and peak power density as a function of load resistance for LIG/CMCS/Acrylic TENG (inset: bridge full-wave rectifier circuit). Charging curve of (h) 0.01 μF and (i) 0.1 μF commercial ceramic capacitors generated by LIG/CMCS/Acrylic TENG.

H/C−O−C), which reveals that the absorption of 10.6 μm (~943 cm^{-1}) CO_2 laser by the CMCS film is mainly related to the vibration absorption behavior of C−O−C/C−O groups. The highly coherent laser can be absorbed by the CMCS and converted into heat energy to create a local environment of high temperature and high pressure, where all the original chemical bonds were broken. The FTIR of generated CMCS-LIG (Figure 4b) shows significant changes in absorption bands (stretching vibration of O−H at 3743 cm^{-1}, stretching vibration of C═C at 1641 and 1566 cm^{-1}, and stretching vibration of C−C/C−O at 1425 cm^{-1}) compared with the mother compound, meaning the formation of new chemical bonds and groups after laser treatment. As two key parameters, the laser powers (from 4.0 to 5.6%) and DLW speeds (from 30 to 150 mm/s) were further selected to control the laser energy density, and the Raman spectrum was employed to monitor the effect of heat accumulation on LIG formation. The conditionally engraved CMCS samples are depicted in Figures S8 and S11. The power-independent Raman spectra (Figure 4c) exhibit that for the ablated CMCS samples with laser power higher than 4.4%, D, G, and 2D peaks of graphene structure can be simultaneously observed, while for the CMCS-4.0% square, there is no obvious 2D characteristic peak of few-layer graphene for single carbonization and lacking a further graphitization. Combined with the sheet resistance variation in Figure 3f, it can be speculated that sufficient laser power density is indispensable for the formation of CMCS-LIG, but too high a power will also reduce the quality of the resulting graphene structure. DLW speed-independent Raman spectra disclose the process of heat-dominated LIG formation from another perspective. As illustrated in Figure 4d, in the ranges of 150−90 mm/s, the curves display weak D and G peaks with strong background levels from CMCS itself, implying incomplete carbonization due to low energy densities at excessive DLW speeds. When the speed reaches 60 mm/s, the D and G peaks of ablated char are further highlighted. For the CMCS-30 mm/s sample obtained at the highest energy density, the D, G, and 2D peaks of LIG can be finally observed. These Raman spectra well verify that the transformation from CMCS to LIG networks is mainly driven by the laser-induced photo-thermal effect, in other words, the chitosan-based molecules with aliphatic repeat units are first carbonized into amorphous chars in relatively low energy density, and can trigger a further graphitization with more sufficient laser energy flux, which is consistent to the mechanism of LIG formation on PI and wood induced by CO_2 laser pyrolysis.[67,68]

For the development of LIG electronics, researchers have made a lot of exploration for polymer precursor materials.[5] Indeed, precursors, as carbon sources, mechanical support, or even functional layers, play multiple critical roles in the syntheses and applications of LIG. With the discovery of different starting materials, relative progress in synthesis mechanism, laser processing method, and advanced applications have been also continuously expanded.[2,11] Figure S12 displays the evolutionary relationship of three different categories of hitherto discovered polymer precursors, and their brief characteristics are listed. As a new family of ecofriendly carbon sources, in comparison with synthetic

https://doi.org/10.1021/acsanm.3c01408
ACS Appl. Nano Mater. 2023, 6, 10453−10465

plastic polymers, chitosan-based polymers feature non-toxicity, biocompatibility, and biodegradability; while compared with lignin/cellulose-based materials, they are often fire retardant and have a measurable and relatively consistent composition, and thus, the corresponding LIG preparation just requires a cost-effective one-step CO_2 laser at ambient atmosphere without any extra pretreatment, multiple lasing recipes, and costly laser devices. It can be said that, to some extent, chitosan-class polymers are well-compatible with the advantages of both plastic polymers and lignocellulose-based substances, achieving an ingenious balance. Chitosan-class polymers effectively expand the family of LIG precursors and provide a new chance for biocompatible and biodegradable LIG electronics. As mentioned in the introduction, laser-induced carbonization can be achieved as well using chitosan-containing materials, but the irregular crab shell suffers from the same problems as some cellulose-based natural materials (such as potatoes). As seen in Figure S13a, although graphitization occurs in local areas, others burn directly into gray-white ashes. In other words, the irregular shape of the shell leads to a visible difference in lased products, and it reveals again that chitosan-based natural raw materials are often not suitable for the large-scale production and systematic study of LIG. It is also worth noting that no obvious carbonization was observed on chitosan-5% acetic acid substrate under any set of conditions (Figure S13b), perhaps because the addition of acetic acid changes the ignition temperature of the prepared composite film.

Chitosan-class polymers also have a series of other metrics as the starting materials. First, the laser-induced graphitization of chitosan-class materials will promote the utilization of renewable chitosan resources. Second, thanks to the good water solubility of most derivatives, except to be prepared into uniform films for the planar compatible process like synthetic plastics, it also provides the possibility of pre-doping of III/V main-group elements (B and P, etc.) or other two-dimensional materials (like MoS_2) during the film preparation to obtain LIG composites with designated improved properties. Third, chitosan-based LIG devices are probably suitable for some edible applications.[42,69] Finally, chitosan-derived polymers have originally been widely studied in the field of bio-electronics and gel-electronics, etc., and therefore, combined with 3D porous LIG, these kinds of composites are expected to apply in more interdisciplinary fields. Of course, their disadvantages are inevitable, for example, these films are relatively easy to absorb moisture in the ambient environment, which means that highly sealed packaging techniques or other measures are required for some humidity-sensitive applications. Moreover, the flexibility of chitosan polymer films is easily affected by the thickness and moisture content, etc., and thus, large-scale uniform products require strict process parameters. In addition, likewise, their mechanical, physical, and chemical stability are relatively weaker than synthetic plastic polymers. These shortcomings need to be further adjusted according to specific applications.

TENG is an advanced and versatile electronic device that can be utilized for environmental energy harvesting and self-powered electronics.[70−72] Chitosan-based polymers have been considered promising and viable alternatives for most-used synthetic plastics to achieve green TENGs and tackle the challenges of recycling e-waste most recently.[73] In this study, to realize the potential electronic application of chitosan derivative LIGs, based on LIG/CMCS film with high mechanical reliability, two different dielectric-to-dielectric TENGs (LIG/CMCS/Acrylic and LIG/CMCS/PI) were constructed, and the corresponding schematic is depicted in Figure 5a. The positive tribo-layer is on the top side and the negative one is on the bottom side, placed parallel to each other face to face and both fixed on the acrylic plates. The top LIG electrode is connected to the ground by an external load, forming a loop through which the current can pass. These as-prepared TENG devices were fixed on the acrylic spring plates (Figure 5b) and tested in a vertical contact-separation (CS) mode (Figure S14). The common CS speed and distance are 500 mm/min and 5 mm, respectively, and a 20 × 20 mm^2 LIG electrode was fabricated on the top of the CMCS substrate (Figure 5b). Figure 5c displays the cross-sectional SEM image of the new-fabricated LIG/CMCS composite film for TENG construction, where the thickness of CMCS film is about 360 μm and there is an approximately 50 μm LIG layer.

As shown in Figure S15a,b, the open-circuit voltages (V_{OC}) generated from the separation and contact processes are ranging from −27.10 to 28.57 V and −22.80 to 28.57 V for LIG/CMCS/Acrylic and LIG/CMCS/PI TENGs, respectively. The corresponding short-circuit currents (I_{SC}) were simultaneously measured (Figure S15c,d), and their values vary from −87.04 to 65.56 nA and −59.78 to 42.00 nA, respectively. It can be seen that, in terms of V_{OC}, there is no obvious difference between LIG/CMCS/Acrylic and LIG/CMCS/PI TENGs, which may be attributed to the strong tribo-negative property of both PI and acrylic and CMCS film with weak triboelectric performance constraints the interface potential difference. For the I_{SC}, however, LIG/CMCS/Acrylic TENGs exhibit greater performance than that of LIG/CSHC/PI, and acrylic seems a better choice to enhance the current, which should be caused by the intrinsic resistance difference between the two TENG devices. Overall, the voltage output signals of all these TENGs are more stable than those of currents.

The schematic diagram in Figure 5d reveals the principle of triboelectric generation, and the labeled V_{OC} and I_{SC} diagrams of LIG/CMCS/Acrylic TENG are used to assist in illustration (Figure 5e,f). In the initial state, the upper and lower tribo-layers are completely separated, and therefore, there is no potential difference between them. When the tribo-positive CMCS gradually contacts the tribo-negative acrylic/PI with a certain pressure (pressed state), contact electrification will occur between their contact interface because of the charge exchange and transfer induced by their triboelectric difference. Since acrylic/PI is more likely to capture electrons than CMCS, acrylic/PI will appear negative due to the extra electrons, and CMCS will accordingly lose an equal amount of electrons and become positive. Notably, the charges on the dielectric material are difficult to form an effective current and can only be bound on both sides of the interface. Therefore, in this stage, due to the electrostatic shielding effect, the potential difference between the two tribo-layers is still zero and no current is generated in the external circuit. Then, the external force is tardily released and the tribo-positive CMCS is gradually separated from the tribo-negative acrylic/PI (releasing state). Consequently, the interface charge will not be completely shielded, and the induced potential difference will be formed. In the external circuit, to balance the electrostatic field, a corresponding positive current will be generated from the LIG electrode to the ground. After complete separation (released state), the peak voltage will be temporarily

https://doi.org/10.1021/acsanm.3c01408
ACS Appl. Nano Mater. 2023, 6, 10453−10465

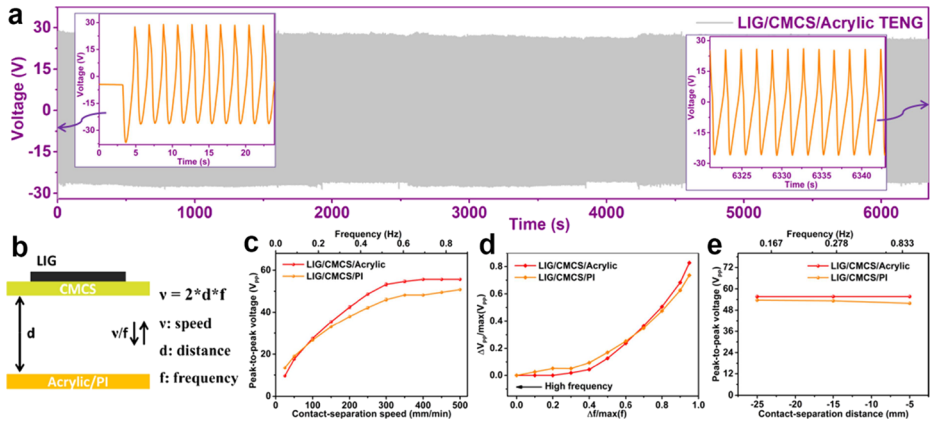

Figure 6. (a) Long-time measurement of LIG/CMCS/Acrylic TENG for ~3200 cycles. (b) TENG model for variable studies. (c) Speed (frequency)-peak-to-peak voltage (V_{PP}) curves of TENGs. (d) Relative V_{PP} variation as a function of frequency change of two different TENGs and the maximum value of frequency and V_{PP} are selected as the references. (e) Distance (frequency)−V_{PP} curves of TENGs.

maintained, and the charge in the external circuit is no longer flowing, so the current returns to zero. When the tribo-layers of the TENG recombine (pressing state), the output voltage will increase in the opposite direction, and at the same time, a negative current peak will be correspondingly generated, and the current flows from the ground to the LIG electrode. These TENGs are continuously cycled so that both voltage and current generations are continuous alternating current signals. Based on this principle and the output voltage results, a comparative triboelectric series of LIG/CMCS, PI, and acrylic can also be obtained (Figure S15e).

Subsequently, the internal resistance and the maximum peak power density of these devices were also experimentally obtained by adding a series of load resistors to the external circuit. Figure S16 is the schematic of the test circuit and the results are plotted in Figure S15f,g. These curves all display a general trend that the peak voltage increases with the enhancement of load resistances, and the peak power densities rise first and then fall. As the load resistances increase from 10 to 1000 MΩ, the peak voltage ranges for LIG/CMCS/Acrylic and LIG/CMCS/PI TENGs are 0.69−26.53 and 0.20−19.30 V, respectively. When the peak power density reaches the maximum value, the corresponding load resistance is equal to the internal resistance of the power source due to the resistance matching. Hence, the maximum peak power density of LIG/CMCS/Acrylic and LIG/CMCS/PI TENGs is approximately 2.48 and 1.44 mW m^{-2}, respectively, and the corresponding internal resistance of them is on the order of 400 MΩ. These results indicate that the fabricated LIG/CMCS composite film exhibits good potential for TENG application.

Chitosan-class polymers and chitosan-based composites have been extensively studied as tribo-positive materials to build low-cost and ecofriendly TENGs (Table S4).[73−76] In terms of charge collection, costly metal films or metal nanomaterials are still the most-used electrodes for almost all chitosan-based TENG devices. The utilization of metal materials also resulted in the generation of solid waste that was not easily disposed of at the end terminal. The present LIG offers a new opportunity for promising TENG electrodes and is more conducive to the environment due to its relatively good environmental compatibility. Compared with relative studies reported before, the power performance of as-presented TENGs with LIG electrodes is very close to or larger than some purely unmodified chitosan-based TENGs with similar structure designs and identical working modes. For example, Kim et al. reported an Al/chitosan/FEP/Al TENG with a maximum power density of 4.24 mW/m^2 at the load resistance level of 100 MΩ,[77] and Wang et al. designed an Al/chitosan/Kapton/Al TENG with a peak power density of 2.1 μW m^{-2} at the same resistance order of 100 MΩ (Table S4).[76] Although the conductivity of the LIG electrode is still smaller than that of its metal counterpart, the intrinsic internal resistance of the TENG device at the megohm level makes this effect almost negligible. The performance of LIG-based TENG devices is further compared. As displayed in Table S5, the power density of LIG/CMCS/Acrylic and LIG/CMCS/PI TENGs is relatively low and is only comparable with LIG/PI/PMMA TENG with a common porous LIG electrode (2.4 W m^{-2}).[78] On the one hand, the positive triboelectric property of the CMCS film is much smaller than that of many plastic films, and the smooth and unmodified surface is also not conducive to the improvement of triboelectric performance. As can be seen from Table S4, it is difficult for unmodified chitosan-based polymer films to improve the performance of triboelectric generation, which is also an important challenge for this class of degradable tribo-positive materials.[73] On the other hand, the morphology and quality of LIGs also affect the power density of TENG. Lee and co-workers have demonstrated that the TENGs based on ordinary porous or short-fiber LIGs (similar to CMCS-LIG, Figure 2b) have significantly weakened triboelectric generation ability compared to the ones with long-fibrous LIGs.[78] Therefore, the main characteristics of both CMCS and LIG layers, including their triboelectric sequence, film feature (such as thickness and flatness), surface microscopic structure, etc., all directly affect the final output performance of as-prepared TENGs.

As these TENGs can effectively collect low-frequency mechanical energy, the superior LIG/CMCS/Acrylic TENG with a bridge full-wave rectifier circuit (Figures 5g and S16) was used to charge two commercial ceramic capacitors. The initial contact force, spacer, and speed for target TENG are ~10 N, 5 mm, and 500 mm/min, respectively. As depicted in Figure 5h,i, the 0.01 μF capacitor can stabilize at 3.73 V after ~35 s of charging, and the larger 0.1 μF one can reach ~0.87 V after charging 20 s. The long-time measurement (Figure 6a) also discloses that the device can generate highly stable voltage output after about 6340 s (~3200 cycles) of continuous

https://doi.org/10.1021/acsanm.3c01408
ACS Appl. Nano Mater. 2023, 6, 10453−10465

working. These results mean that the as-fabricated chitosan polymer-based TENGs with LIG electrodes have stable and fast abilities to collect low-frequency mechanical energy in the environment, which is expected to power the rapidly increasing number of intelligent sensing nodes of the wireless sensor network (WSN) and reduce the dependence on energy storage devices such as batteries in the Internet of Things (IoT) era.

Finally, the impact of frequency (f) and CS distance (d) on the output performance of the TENGs was evaluated in more depth. The effect of frequency was explored first when keeping the initial pressure of ∼10 N and a CS distance of 5 mm. The frequency change was achieved by maintaining the distance while setting different motor speeds (ν) based on the formula: $f = \nu/2d$ (Figure 6b). The output voltage was chosen as the dependent variable because of its periodic stable signal. As can be seen from Figures S17a,b and 6c, for these TENGs, with the gradual increase of CS speeds from 25 to 500 mm/min or frequencies from 0.042 to 0.833 Hz, the output voltages correspondingly rise ranging from 9.61 to 55.67 V and 13.42 to 50.79 V for LIG/CMCS/Acrylic and LIG/CMCS/PI TENGs, respectively. It is also indicated that all these devices can efficiently capture mechanical energy even at exceptionally low frequencies (0.042 Hz), and the output signals are still stable. This frequency−voltage relationship could be ascribed to that the contact or separation of two tribo-layers is accelerated at a relatively higher operating frequency, and the rapid transfer of the induced charges leads to the boost of charge density and current. In the non-ideal open-circuit state, the voltage has a similar response. Nevertheless, there is a limit to this effect, and the peak-to-peak voltage (V_{PP}) will gradually tend to saturation (Figure 6f). As the frequency approaches the maximum set value, LIG/CMCS/Acrylic TENG has shown significant voltage saturation, while another one maintains a slight upward trend. Given the positive correlation between frequency and V_{PP}, these TENGs can also realize voltage-type frequency sensing functions. Therefore, after further data processing, the curve of V_{PP} variation ($\Delta V_{PP}/\max(V_{PP})$) with frequency change ($\Delta f/\max(f)$) is shown in Figure 6d, where the highest frequency and its corresponding V_{PP} are selected as the references. The slope changes reveal that these devices have higher gauge factors (GF, the slope of the curves) in the low-frequency region, and the GF will approach zero as the frequency gradually increases to the maximum reference value, which means that the frequency change in the low-frequency range will cause a more pronounced voltage variation. In the low-frequency interval, where $\Delta f/\max(f)$ belongs to (0.9, 0.95), the maximum GF value of LIG/CMCS/Acrylic and LIG/CMCS/PI is 0.16 and 0.12, respectively, indicating an excellent voltage response of these voltage-type TENGs for mechanical frequency changes.

Based on the same initial pressure (∼10 N) and CS speed (500 mm/min), their output voltages at different distances were also measured. The results are displayed in Figure S17c,d and further collated in Figure 6e. As the interval decreases linearly (minus just means direction), the frequency also decreases in an inversely proportional function on account of $d = \nu/2f$, therefore, the effects of both distance and frequency should be considered simultaneously. As the spacer ascends from 5 to 25 mm, the V_{PP} of LIG/CMCS/Acrylic TENG remains constant at 55.67 V and that of LIG/CMCS/PI also climbs from 51.87 to 53.65 V with a very small slope. From another perspective, a relatively stable voltage response corresponds to a very sharp frequency change from 0.84 to 0.14 Hz. It could be validly inferred that in the range of 5−25 mm, the distance factor plays a more critical role in the output performance than frequency, and especially for LIG/CMCS/Acrylic TENG, only a spacer of 5 mm can saturate the output voltage. This positive distance−voltage effect could attribute to the fact that the induced potential difference grows with the spacer, which promotes the flow of electrons in the external circuit and thus improves the triboelectric output of TENGs. These variable studies (Figure 6c−e) reveal that whether PI or acrylic was a tribo-negative dielectric layer, the devices responded to parameter changes in a highly consistent way, thus demonstrating the high reliability and reusable capability of the LIG/CMCS composite film.

CONCLUSIONS

In summary, chitosan-class derivatives are discovered as the new generation of ecofriendly LIG carbon precursors, and based on the as-fabricated CMCS, COS, and CSHC films, the desired LIG products can be easily obtained using a facile one-step CO_2 laser in the ambient atmosphere. The physicochemical and interface properties of as-obtained CMCS-LIG, COS-LIG, and CSHC-LIG are also characterized. The results exhibit that they are featured by the obvious 3D hierarchical porous structure and super-hydrophilic interface property and possess excellent sheet resistance performance (33.9 Ω sq^{-1} for COS-LIG and 12.7 Ω sq^{-1} for CSHC-LIG), which are comparable to other carbon precursor-derived LIGs. The consecutive carbonization and graphitization mechanism of chitosan derivatives are also experimentally monitored, and the formation of LIG is directly related to the heat accumulation produced by laser irradiation. In addition, based on the mechanically reliable LIG/CMCS film, LIG/CMCS/Acrylic and LIG/CMCS/PI TENGs are built, and their maximum power densities are 2.48 and 1.44 mW m^{-2}, respectively. These devices can achieve stable low-frequency mechanical energy harvesting and variable-controlled sensing, which is expected to be used in WSN nodes and the IoT network. In brief, the successful laser pyrolysis of chitosan-class derivatives in this work will effectively expand the family of LIG precursors and pave a brand-new way toward biofriendly LIG electronics.

EXPERIMENTAL SECTION

Reagents. Chitosan (DD ≥ 95%, Macklin), CMCS (BR, Macklin), COS (MW < 3000, Shanghai yuanye Bio-Technology Co., Ltd), CSHC (DD ≥ 95%, Macklin), and 36% acetic acid (CH_3COOH, AR, Aladdin). All these reagents were used as received and not further purified. Cautions: High concentrations of the acetic acid solution have a strong pungent smell, so it should be used in a ventilated place, and wear a protective mask. (Abbreviations: DD, degree of deacetylation; BR, biochemical reagent; MW, molecular weight; and AR, analytical reagent.)

Film Fabrication. As the powder of chitosan derivative reagents has very good water solubility, the films used in the experiment were prepared by a simple thermal evaporation method. The main preparation process is shown in Figure 1b. For the CMCS film, 10 g of CMCS powder was dissolved in 100 mL of deionized water in a beaker and constantly stirred with a glass bar. After complete dissolution, the highly viscous solution with numerous bubbles was degassed for 3−5 min using a vacuum freeze dryer, and uniform CMCS solution can be obtained. As-prepared CMCS solution (15 mL) was extracted with a 5 mL pipette and injected into a 66 mm diameter circular plastic container, and then transferred to a 333 K (60 °C) vacuum drying tank. After 48−72 h, dry and flat CMCS films were available. For CSHC film, the fabrication process is very similar to that of CMCS film, and only the deionized water needs to be

https://doi.org/10.1021/acsanm.3c01408
ACS Appl. Nano Mater. 2023, 6, 10453−10465

decreased to 110 mL, respectively. For the chitosan film, 150 mL of 5% acetic acid solution was needed as a solvent. For COS film, due to the low molecular weight and relatively high solubility of COS, 10 g of powder requires only 100 mL of deionized water. In addition, the viscosity of the solution was very low, so the degassing operation could be achieved by a simple static placement. The obtained films are displayed in Figures 1c and S13b, and all of these films prepared for this work are thicker than 500 μm. It should be noted that COS and CSHC films are prone to deformation and brittle cracking due to their sensitivity to stress and high brittleness, and this change can be slowly intensified in the ambient environment. Therefore, they need to be tailored in advance for further laser pyrolysis experiments.

Lasing Induction of LIGs. All these prepared chitosan-based films were irradiated by a commercial 10.6 μm infrared CO_2 laser engraver (Hui-Bang Laser Technology's Taobao store) using the planar processing method. First, the film to be processed was fixed on a working platform below the laser head, and then the pattern to be carved was drawn on the DrawChem software. When the parameters were set, the laser engraving process can transfer the designed pattern onto the film substrate and generate LIG material within the designed shape. This continuous wave laser machine adopts a linear scanning swing mode, and its rated power and positioning accuracy is 40 W and ≤0.01 mm, respectively. Its main adjustable parameters include laser power, scanning speed, pixel step, the distance between the laser source and substrate, etc. In this study, unless otherwise stated, a slow scan speed of 30 mm/s and a small pixel step of 2 were set to constant, and each substrate to be treated was roughly placed at the focal plane (10 mm below the laser head). Considering the data reliability, the laser power was expressed by the duty cycle, and the theoretical power value can be obtained by multiplying the duty cycle and rated power. The laser power was regulated in the range of 4−6%, and besides, all the experiments were conducted under ambient conditions (temperature: ∼25 °C, humidity: ∼50%).

LIG Characterizations. The optical paragraphs with relatively low magnifications were obtained via the mobile phone camera or normal photo microscope. The surface morphology of as-fabricated LIGs was obtained by secondary electron SEM (Regulus SU8230) with an accelerating voltage of 5 kV, and the samples were gold-sprayed before imaging to enhance the surface conductivity. The TEM (TECNAI G2F30, Thermo Fisher) measurements were performed at an accelerating voltage of 300 kV. For TEM imaging, the LIG samples were scratched from the surface of substrates and then dispersed into an absolute alcohol solution with an ultrasonic process of 20 min. After that, each LIG-containing sample solution was dripped into 200 meshes of the copper grid with a supporting carbon membrane for observation. The resulting TEM images were processed by DigtalMicrograph software. Raman spectra were recorded via the Laser Confocal Raman Spectrometer (LabRAM HR Evolution) with a 532 nm incident laser at room temperature. The surface chemical analysis of substrate films and synthesized LIG samples were acquired by the XPS apparatus (PHI 5000 Versaprobe III, ULVAC-PHI) with an Al Kα X-ray source and a base pressure of 10^{-7} Torr. The fine C spectra were recorded in 0.125 eV step size with the pass energy of 69 eV and corrected using contaminated C1s peak (284.8 eV) as the reference. The wettability of water to the LIG interface was tested with a contact angle meter (Dongguan Shengding Precision Instrument Co., Ltd.). Sheet resistance measurements were achieved by the four-point van der Pauw approach using a Keithley Model 2450 System SourceMeter, and each charred square was measured in triplicate and the corresponding mean values were calculated. The FTIR spectrum was recorded by a fully digital FTIR spectrometer (VERTEX 70v).

TENG Fabrication. Two dielectric-to-dielectric TENGs were fabricated in a vertical CS type. The CMCS film with the lased LIG electrode was used as the tribo-positive layer, and the square LIG electrode (20 × 20 mm^2) was prepared by a single-step laser engraving method with a laser power of 5.2%. The tribo-negative material was selected from an acrylic plate (286 mm) or the PI film (0.25 mm). The main body of the device was assembled by two acrylic plates, four acrylic pillars, and four retractable springs, as shown in Figure 5b. The upper plate supported by the springs can complete the CS behavior under vertical pressures. For LIG/CMCS/Acrylic TENG, the LIG/CMCS composite was fixed to the lower side of the upper acrylic plate, while the lower acrylic plate acted directly as the tribo-negative layer. In addition, for LIG/CMCS/PI TENG, an additional PI film was attached to the surface of the underlying acrylic plate as a counterbalance layer. To facilitate the electrical testing of these TENGs, the LIG electrode was further connected to a copper wire via conductive silver paste and was well encapsulated with plastic tape. The contact between the TENG device and the external testing circuit was achieved by standard electrical alligator clips.

TENG Characterization. The output voltage and current of the TENGs were measured using a Keithley 6517B electrometer, and the corresponding data were collected by a Keithley Model 2450 System SourceMeter with a Kingstar software package. The CS action was controlled by a push-and-pull system (Shenzhen Wance Testing Machine Co., Ltd.). The speed and distance of CS behavior can be customized, and their typical values are 500 mm/min and −5 mm, respectively. The output voltage at different CS speeds and distances was also investigated for deep research. The initial contact force between the upper and lower tribo-layers is about 10 N for these TENGs at each measurement. The peak power density versus load resistance curves was also obtained by adding a series of load resistances (10, 50, 100, 200, 300, 400, 500, 600, 700, 800, 900, and 1000 MΩ, supplied by a resistance box) in the external circuit. The peak voltages of the load resistances were obtained via direct measurement, while the peak power density (P_P) was further calculated through the formula: $P_P = V_P^2/RA$, where V_P is the peak voltage, R devotes the load resistance, and A devotes the area of LIG electrodes.

■ ASSOCIATED CONTENT

Supporting Information

The Supporting Information is available free of charge at https://pubs.acs.org/doi/10.1021/acsanm.3c01408.

Structure relationship of chitosan-class polymers, Raman spectra, high-resolution TEM images, XPS spectra, optical photographs of lased LIGs, the TENG test system and output performance, charging curves, and some statistical tables derived from Raman spectra, XPS spectra, sheet resistance, LIG-based TENGs, and chitosan polymer-based TENGs (PDF)

■ AUTHOR INFORMATION

Corresponding Author

Huaiyu Ye − *School of Microelectronics, Southern University of Science and Technology, Shenzhen 518055, China; Electronic Components, Technology and Materials, Delft University of Technology, 2628 CD Delft, The Netherlands;* orcid.org/0000-0002-0385-4728; Email: h.ye@tudelft.nl

Authors

Qian-Ming Huang − *Harbin Institute of Technology, Harbin 150001, China; School of Microelectronics, Southern University of Science and Technology, Shenzhen 518055, China*

Huiru Yang − *Harbin Institute of Technology, Harbin 150001, China; School of Microelectronics, Southern University of Science and Technology, Shenzhen 518055, China*

Shaogang Wang − *School of Microelectronics, Southern University of Science and Technology, Shenzhen 518055, China; Electronic Components, Technology and Materials, Delft University of Technology, 2628 CD Delft, The Netherlands*

Xu Liu − *School of Microelectronics, Southern University of Science and Technology, Shenzhen 518055, China; Electronic Components, Technology and Materials, Delft University of Technology, 2628 CD Delft, The Netherlands*
Chunjian Tan − *School of Microelectronics, Southern University of Science and Technology, Shenzhen 518055, China; Electronic Components, Technology and Materials, Delft University of Technology, 2628 CD Delft, The Netherlands*
Anxin Luo − *School of Microelectronics, Southern University of Science and Technology, Shenzhen 518055, China*
Siyuan Xu − *School of Microelectronics, Southern University of Science and Technology, Shenzhen 518055, China*
Guoqi Zhang − *Electronic Components, Technology and Materials, Delft University of Technology, 2628 CD Delft, The Netherlands*

Complete contact information is available at: https://pubs.acs.org/10.1021/acsanm.3c01408

Author Contributions

Q.M.H. designed and performed all the experiments, analyzed data, and wrote the manuscript. H.Y, S.W., X.L., C.T., A.L., and S.X. provided plenty of constructive ideas and valuable discussions. H.Y. and G.Z. guided the research. All authors have approved the final version of the manuscript.

Notes

The authors declare no competing financial interest.

■ ACKNOWLEDGMENTS

This work was supported by the National Key R&D Program of China (2018YFE0204600), the Shenzhen Fundamental Research Program (JCYJ20200109140822796), and Special Funds for the Cultivation of Guandong College Students' Scientific and Technological Innovation (pdjh 2022c0080). Thanks to Professor Kwai Hei Li's group for their help in the contact angle measurements. Thanks to the WeChat official accounts "PPT kyht" and "ke-yan-gong-jin-she", and some webpages ("You pin PPT" and Pixabay) for their free PPT and picture materials.

■ REFERENCES

(1) Ye, R.; James, D. K.; Tour, J. M. Laser-Induced Graphene. *Acc. Chem. Res.* **2018**, *51*, 1609−1620.
(2) Ye, R.; James, D. K.; Tour, J. M. Laser-Induced Graphene: From Discovery to Translation. *Adv. Mater.* **2019**, *31*, No. 1803621.
(3) Ye, X.; Long, J.; Lin, Z.; Zhang, H.; Zhu, H.; Zhong, M. Direct laser fabrication of large-area and patterned graphene at room temperature. *Carbon* **2014**, *68*, 784−790.
(4) Duy, L. X.; Peng, Z.; Li, Y.; Zhang, J.; Ji, Y.; Tour, J. M. Laser-induced graphene fibers. *Carbon* **2018**, *126*, 472−479.
(5) Le, T. S. D.; Phan, H. P.; Kwon, S.; Park, S.; Jung, Y.; Min, J.; Chun, B. J.; Yoon, H.; Ko, S. H.; Kim, S. W.; Kim, Y. J. Recent Advances in Laser-Induced Graphene: Mechanism, Fabrication, Properties, and Applications in Flexible Electronics. *Adv. Funct. Mater.* **2022**, *32*, No. 2205158.
(6) Wang, Y.; Zhao, Y.; Li, X.; Jiang, L.; Qu, L. Laser-Based Growth and Treatment of Graphene for Advanced Photo-and Electro-Related Device Applications. *Adv. Funct. Mater.* **2022**, *32*, No. 2203164.
(7) Kumar, R.; Pérez del Pino, A.; Sahoo, S.; Singh, R. K.; Tan, W. K.; Kar, K. K.; Matsuda, A.; Joanni, E. Laser processing of graphene and related materials for energy storage: State of the art and future prospects. *Prog. Energy Combust. Sci.* **2022**, *91*, No. 100981.
(8) Liu, H.; Sun, Z.; Chen, Y.; Zhang, W.; Chen, X.; Wong, C. P. Laser Processing of Flexible In-Plane Micro-supercapacitors: Progresses in Advanced Manufacturing of Nanostructured Electrodes. *ACS Nano* **2022**, *16*, 10088−10129.
(9) Vivaldi, F. M.; Dallinger, A.; Bonini, A.; Poma, N.; Sembranti, L.; Biagini, D.; Salvo, P.; Greco, F.; Di Francesco, F. Three-Dimensional (3D) Laser-Induced Graphene: Structure, Properties, and Application to Chemical Sensing. *ACS Appl. Mater. Interfaces* **2021**, *13*, 30245−30260.
(10) Alhajji, E.; Zhang, F.; Alshareef, H. N. Status and Prospects of Laser-Induced Graphene for Battery Applications. *Energy Technol.* **2021**, *9*, No. 2100454.
(11) You, R.; Liu, Y. Q.; Hao, Y. L.; Han, D. D.; Zhang, Y. L.; You, Z. Laser Fabrication of Graphene-Based Flexible Electronics. *Adv. Mater.* **2020**, *32*, No. 1901981.
(12) Kurra, N.; Jiang, Q.; Nayak, P.; Alshareef, H. N. Laser-derived graphene: A three-dimensional printed graphene electrode and its emerging applications. *Nano Today* **2019**, *24*, 81−102.
(13) Kumar, R.; Singh, R. K.; Singh, D. P.; Joanni, E.; Yadav, R. M.; Moshkalev, S. A. Laser-assisted synthesis, reduction and micro-patterning of graphene: Recent progress and applications. *Coord. Chem. Rev.* **2017**, *342*, 34−79.
(14) Peng, Z.; Ye, R.; Mann, J. A.; Zakhidov, D.; Li, Y.; Smalley, P. R.; Lin, J.; Tour, J. M. Flexible Boron-Doped Laser-Induced Graphene Microsupercapacitors. *ACS Nano* **2015**, *9*, 5868−5875.
(15) Ye, R.; Peng, Z.; Wang, T.; Xu, Y.; Zhang, J.; Li, Y.; Nilewski, L. G.; Lin, J.; Tour, J. M. In Situ Formation of Metal Oxide Nanocrystals Embedded in Laser-Induced Graphene. *ACS Nano* **2015**, *9*, 9244−9251.
(16) Lamberti, A.; Clerici, F.; Fontana, M.; Scaltrito, L. A Highly Stretchable Supercapacitor Using Laser-Induced Graphene Electrodes onto Elastomeric Substrate. *Adv. Energy Mater.* **2016**, *6*, No. 1600050.
(17) Thamaraiselvan, C.; Wang, J.; James, D. K.; Narkhede, P.; Singh, S. P.; Jassby, D.; Tour, J. M.; Arnusch, C. J. Laser-induced graphene and carbon nanotubes as conductive carbon-based materials in environmental technology. *Mater. Today* **2020**, *34*, 115−131.
(18) Huang, Y.; Tao, L.-Q.; Yu, J.; Zheng, K.; Wang, G.; Chen, X. Improved Performance of Flexible Graphene Heater Based on Repeated Laser Writing. *IEEE Electron Device Lett.* **2020**, *41*, 501−504.
(19) Huang, Y.; Tao, L. Q.; Yu, J.; Wang, Z.; Zhu, C.; Chen, X. Integrated Sensing and Warning Multifunctional Devices Based on the Combined Mechanical and Thermal Effect of Porous Graphene. *ACS Appl. Mater. Interfaces* **2020**, *12*, 53049−53057.
(20) Ge, L.; Hong, Q.; Li, H.; Liu, C.; Li, F. Direct-Laser-Writing of Metal Sulfide-Graphene Nanocomposite Photoelectrode toward Sensitive Photoelectrochemical Sensing. *Adv. Funct. Mater.* **2019**, *29*, No. 1904000.
(21) Xu, Y.; Fei, Q.; Page, M.; Zhao, G.; Ling, Y.; Chen, D.; Yan, Z. Laser-induced graphene for bioelectronics and soft actuators. *Nano Res.* **2021**, *14*, 3033−3050.
(22) Li, J. T.; Stanford, M. G.; Chen, W.; Presutti, S. E.; Tour, J. M. Laminated Laser-Induced Graphene Composites. *ACS Nano* **2020**, *14*, 7911−7919.
(23) Lin, J.; Peng, Z.; Liu, Y.; Ruiz-Zepeda, F.; Ye, R.; Samuel, E. L.; Yacaman, M. J.; Yakobson, B. I.; Tour, J. M. Laser-induced porous graphene films from commercial polymers. *Nat. Commun.* **2014**, *5*, 5714.
(24) Kaidarova, A.; Kosel, J. Physical Sensors Based on Laser-Induced Graphene: A Review. *IEEE Sens. J.* **2021**, *21*, 12426−12443.
(25) Li, L.; Zhang, J.; Peng, Z.; Li, Y.; Gao, C.; Ji, Y.; Ye, R.; Kim, N. D.; Zhong, Q.; Yang, Y.; Fei, H.; Ruan, G.; Tour, J. M. High-Performance Pseudocapacitive Microsupercapacitors from Laser-Induced Graphene. *Adv. Mater.* **2016**, *28*, 838−845.
(26) Beckham, J. L.; Li, J. T.; Stanford, M. G.; Chen, W.; McHugh, E. A.; Advincula, P. A.; Wyss, K. M.; Chyan, Y.; Boldman, W. L.; Rack, P. D.; Tour, J. M. High-Resolution Laser-Induced Graphene from Photoresist. *ACS Nano* **2021**, *15*, 8976−8983.
(27) Luong, D. X.; Yang, K.; Yoon, J.; Singh, S. P.; Wang, T.; Arnusch, C. J.; Tour, J. M. Laser-Induced Graphene Composites as Multifunctional Surfaces. *ACS Nano* **2019**, *13*, 2579−2586.

(28) Yi, C.; Hou, Y.; He, K.; Li, W.; Li, N.; Wang, Z.; Yang, B.; Xu, S.; Wang, H.; Gao, C.; Wang, Z.; Gu, G.; Wang, Z.; Wei, L.; Yang, C.; Chen, M. Highly Sensitive and Wide Linear-Response Pressure Sensors Featuring Zero Standby Power Consumption under Bending Conditions. *ACS Appl. Mater. Interfaces* **2020**, *12*, 19563−19571.
(29) Stanford, M. G.; Li, J. T.; Chyan, Y.; Wang, Z.; Wang, W.; Tour, J. M. Laser-Induced Graphene Triboelectric Nanogenerators. *ACS Nano* **2019**, *13*, 7166−7174.
(30) Yan, Z.; Wang, L.; Xia, Y.; Qiu, R.; Liu, W.; Wu, M.; Zhu, Y.; Zhu, S.; Jia, C.; Zhu, M.; Cao, R.; Li, Z.; Wang, X. Flexible High-Resolution Triboelectric Sensor Array Based on Patterned Laser-Induced Graphene for Self-Powered Real-Time Tactile Sensing. *Adv. Funct. Mater.* **2021**, *31*, No. 2100709.
(31) Jiang, C.; Li, X.; Yao, Y.; Lan, L.; Shao, Y.; Zhao, F.; Ying, Y.; Ping, J. A multifunctional and highly flexible triboelectric nanogenerator based on MXene-enabled porous film integrated with laser-induced graphene electrode. *Nano Energy* **2019**, *66*, No. 104121.
(32) Rathinam, K.; Singh, S. P.; Li, Y.; Kasher, R.; Tour, J. M.; Arnusch, C. J. Polyimide derived laser-induced graphene as adsorbent for cationic and anionic dyes. *Carbon* **2017**, *124*, 515−524.
(33) Singh, S. P.; Li, Y.; Zhang, J.; Tour, J. M.; Arnusch, C. J. Sulfur-Doped Laser-Induced Porous Graphene Derived from Polysulfone-Class Polymers and Membranes. *ACS Nano* **2018**, *12*, 289−297.
(34) Wang, F.; Duan, W.; Wang, K.; Dong, X.; Gao, M.; Zhai, Z.; Mei, X.; Lv, J.; Wang, W.; Zhu, C. Graphitized hierarchically porous carbon nanosheets derived from bakelite induced by high-repetition picosecond laser. *Appl. Surf. Sci.* **2018**, *450*, 155−163.
(35) Zhu, C.; Zhao, D.; Wang, K.; Dong, X.; Duan, W.; Wang, F.; Gao, M.; Zhang, G. Direct laser writing of graphene films from a polyether ether ketone precursor. *J. Mater. Sci.* **2018**, *54*, 4192−4201.
(36) Getachew, B. A.; Bergsman, D. S.; Grossman, J. C. Laser-Induced Graphene from Polyimide and Polyethersulfone Precursors as a Sensing Electrode in Anodic Stripping Voltammetry. *ACS Appl. Mater. Interfaces* **2020**, *12*, 48511−48517.
(37) Kong, D.; Kang, M.; Kim, K. Y.; Jang, J.; Cho, J.; In, J. B.; Lee, H. Hierarchically Structured Laser-Induced Graphene for Enhanced Boiling on Flexible Substrates. *ACS Appl. Mater. Interfaces* **2020**, *12*, 37784−37792.
(38) Vashisth, A.; Kowalik, M.; Gerringer, J. C.; Ashraf, C.; van Duin, A. C. T.; Green, M. J. ReaxFF Simulations of Laser-Induced Graphene (LIG) Formation for Multifunctional Polymer Nanocomposites. *ACS Appl. Nano Mater.* **2020**, *3*, 1881−1890.
(39) Dong, Y.; Rismiller, S. C.; Lin, J. Molecular dynamic simulation of layered graphene clusters formation from polyimides under extreme conditions. *Carbon* **2016**, *104*, 47−55.
(40) Ye, R.; Chyan, Y.; Zhang, J.; Li, Y.; Han, X.; Kittrell, C.; Tour, J. M. Laser-Induced Graphene Formation on Wood. *Adv. Mater.* **2017**, *29*, No. 1702211.
(41) Li, Q.; Guo, X.; Zhang, Y.; Zhang, W.; Ge, C.; Zhao, L.; Wang, X.; Zhang, H.; Chen, J.; Wang, Z.; Sun, L. Porous graphene paper for supercapacitor applications. *J. Mater. Sci. Technol.* **2017**, *33*, 793−799.
(42) Chyan, Y.; Ye, R.; Li, Y.; Singh, S. P.; Arnusch, C. J.; Tour, J. M. Laser-Induced Graphene by Multiple Lasing: Toward Electronics on Cloth, Paper, and Food. *ACS Nano* **2018**, *12*, 2176−2183.
(43) de Araujo, W. R.; Frasson, C. M. R.; Ameku, W. A.; Silva, J. R.; Angnes, L.; Paixao, T. Single-Step Reagentless Laser Scribing Fabrication of Electrochemical Paper-Based Analytical Devices. *Angew. Chem. Int. Ed.* **2017**, *56*, 15113−15117.
(44) Zang, X.; Shen, C.; Chu, Y.; Li, B.; Wei, M.; Zhong, J.; Sanghadasa, M.; Lin, L. Laser-Induced Molybdenum Carbide-Graphene Composites for 3D Foldable Paper Electronics. *Adv. Mater.* **2018**, *30*, No. e1800062.
(45) Zhao, P.; Bhattacharya, G.; Fishlock, S. J.; Guy, J. G. M.; Kumar, A.; Tsonos, C.; Yu, Z.; Raj, S.; McLaughlin, J. A.; Luo, J.; Soin, N. Replacing the metal electrodes in triboelectric nanogenerators: High-performance laser-induced graphene electrodes. *Nano Energy* **2020**, *75*, No. 104958.
(46) Kulyk, B.; Silva, B. F. R.; Carvalho, A. F.; Silvestre, S.; Fernandes, A. J. S.; Martins, R.; Fortunato, E.; Costa, F. M. Laser-Induced Graphene from Paper for Mechanical Sensing. *ACS Appl. Mater. Interfaces* **2021**, *13*, 10210−10221.
(47) Yao, Y.; Duan, X.; Niu, M.; Luo, J.; Wang, R.; Liu, T. One-step process for direct laser writing carbonization of NH4H2PO4 treated cellulose paper and its use for facile fabrication of multifunctional force sensors with corrugated structures. *Cellulose* **2019**, *26*, 7423−7435.
(48) Lee, S.; Jeon, S. Laser-Induced Graphitization of Cellulose Nanofiber Substrates under Ambient Conditions. *ACS Sustainable Chem. Eng.* **2018**, *7*, 2270−2275.
(49) Rinaudo, M. Chitin and chitosan: Properties and applications. *Prog. Polym. Sci.* **2006**, *31*, 603−632.
(50) Pillai, C. K. S.; Paul, W.; Sharma, C. P. Chitin and chitosan polymers: Chemistry, solubility and fiber formation. *Prog. Polym. Sci.* **2009**, *34*, 641−678.
(51) Kean, T.; Thanou, M. Biodegradation, biodistribution and toxicity of chitosan. *Adv. Drug Deliv. Rev.* **2010**, *62*, 3−11.
(52) Roy, B. K.; Tahmid, I.; Rashid, T. U. Chitosan-based materials for supercapacitor applications: a review. *J. Mater. Chem. A* **2021**, *9*, 17592−17642.
(53) Wang, H.; Qian, J.; Ding, F. Emerging Chitosan-Based Films for Food Packaging Applications. *J. Agric. Food Chem.* **2018**, *66*, 395−413.
(54) Ma, X.; Wu, N.; Liu, P.; Cui, H. Fabrication of highly efficient phenylphosphorylated chitosan bio-based flame retardants for flammable PLA biomaterial. *Carbohydr. Polym.* **2022**, *287*, No. 119317.
(55) Chen, R.; Luo, Z.; Yu, X.; Tang, H.; Zhou, Y.; Zhou, H. Synthesis of chitosan-based flame retardant and its fire resistance in epoxy resin. *Carbohydr. Polym.* **2020**, *245*, No. 116530.
(56) Zheng, B.; Zhao, G.; Yan, Z.; Xie, Y.; Lin, J. Direct Freeform Laser Fabrication of 3D Conformable Electronics. *Adv. Funct. Mater.* **2023**, *33*, No. 2210084.
(57) Bokobza, L.; Bruneel, J.-L.; Couzi, M. Raman Spectra of Carbon-Based Materials (from Graphite to Carbon Black) and of Some Silicone Composites. *C* **2015**, *1*, 77−94.
(58) Hao, Y.; Wang, Y.; Wang, L.; Ni, Z.; Wang, Z.; Wang, R.; Koo, C. K.; Shen, Z.; Thong, J. T. Probing layer number and stacking order of few-layer graphene by Raman spectroscopy. *Small* **2010**, *6*, 195−200.
(59) Le, T. S. D.; Lee, Y. A.; Nam, H. K.; Jang, K. Y.; Yang, D.; Kim, B.; Yim, K.; Kim, S. W.; Yoon, H.; Kim, Y. J. Green Flexible Graphene-Inorganic-Hybrid Micro-Supercapacitors Made of Fallen Leaves Enabled by Ultrafast Laser Pulses. *Adv. Funct. Mater.* **2022**, *32*, No. 2107768.
(60) Li, Y.; Luong, D. X.; Zhang, J.; Tarkunde, Y. R.; Kittrell, C.; Sargunaraj, F.; Ji, Y.; Arnusch, C. J.; Tour, J. M. Laser-Induced Graphene in Controlled Atmospheres: From Superhydrophilic to Superhydrophobic Surfaces. *Adv. Mater.* **2017**, *29*, No. 1700496.
(61) Misra, U.; Dixit, N.; Singh, S. P. Effect of Laser Parameters on Laser-Induced Graphene Filter Fabrication and Its Performance for Desalination and Water Purification. *ACS Appl. Mater. Interfaces* **2023**, *15*, 7899−7910.
(62) Yan, W. R.; Hu, H. B.; Wang, L.; Ho, D. Dual Defocused Laser Pyrolysis: A Lasing-Centric Strategy for Defect and Morphological Optimization in Microsupercapacitor Electrodes. *Small Methods* **2022**, *6*, No. e2101616.
(63) Liu, H.; Xie, Y.; Li, J.; Sun, Z.; Liu, J.; Moon, K.-S.; Lu, L.; Chen, Y.; Tang, Y.; Chen, X.; Wong, C.-P. Laser-induced nitrogen-self-doped graphite nanofibers from cyanate ester for on-chip micro-supercapacitors. *Chem. Eng. J.* **2021**, *404*, No. 126375.
(64) Nasser, J.; Lin, J.; Zhang, L.; Sodano, H. A. Laser induced graphene printing of spatially controlled super-hydrophobic/hydrophilic surfaces. *Carbon* **2020**, *162*, 570−578.
(65) Tittle, C. M.; Yilman, D.; Pope, M. A.; Backhouse, C. J. Robust Superhydrophobic Laser-Induced Graphene for Desalination Applications. *Adv. Mater. Technol.* **2018**, *3*, No. 1700207.

https://doi.org/10.1021/acsanm.3c01408
ACS Appl. Nano Mater. 2023, 6, 10453−10465

(66) Zhu, J.; Huang, X.; Song, W. Physical and Chemical Sensors on the Basis of Laser-Induced Graphene: Mechanisms, Applications, and Perspectives. *ACS Nano* **2021**, *15*, 18708−18741.
(67) Le, T. S. D.; Park, S.; An, J.; Lee, P. S.; Kim, Y. J. Ultrafast Laser Pulses Enable One-Step Graphene Patterning on Woods and Leaves for Green Electronics. *Adv. Funct. Mater.* **2019**, *29*, No. 1902771.
(68) Zhao, L.; Liu, Z.; Chen, D.; Liu, F.; Yang, Z.; Li, X.; Yu, H.; Liu, H.; Zhou, W. Laser Synthesis and Microfabrication of Micro/Nanostructured Materials Toward Energy Conversion and Storage. *Nanomicro Lett.* **2021**, *13*, 49.
(69) Yan, K.; Li, X.; Wang, X.-X.; Yu, M.; Fan, Z.; Ramakrishna, S.; Hu, H.; Long, Y.-Z. A non-toxic triboelectric nanogenerator for baby care applications. *J. Mater. Chem. A* **2020**, *8*, 22745−22753.
(70) Wang, S.; Lin, L.; Wang, Z. L. Triboelectric nanogenerators as self-powered active sensors. *Nano Energy* **2015**, *11*, 436−462.
(71) Zhang, C.; Wang, Z. L. Tribotronics—A new field by coupling triboelectricity and semiconductor. *Nano Today* **2016**, *11*, 521−536.
(72) Liu, Z.; Li, H.; Shi, B.; Fan, Y.; Wang, Z. L.; Li, Z. Wearable and Implantable Triboelectric Nanogenerators. *Adv. Funct. Mater.* **2019**, *29*, No. 1808820.
(73) Torres, F. G.; De-la-Torre, G. E. Polysaccharide-based triboelectric nanogenerators: A review. *Carbohydr. Polym.* **2021**, *251*, No. 117055.
(74) Sun, J.; Choi, H.; Cha, S.; Ahn, D.; Choi, M.; Park, S.; Cho, Y.; Lee, J.; Park, T. E.; Park, J. J. Highly Enhanced Triboelectric Performance from Increased Dielectric Constant Induced by Ionic and Interfacial Polarization for Chitosan Based Multi-Modal Sensing System. *Adv. Funct. Mater.* **2022**, *32*, No. 2109139.
(75) Zheng, Q.; Fang, L.; Guo, H.; Yang, K.; Cai, Z.; Meador, M. A. B.; Gong, S. Highly Porous Polymer Aerogel Film-Based Triboelectric Nanogenerators. *Adv. Funct. Mater.* **2018**, *28*, No. 1706365.
(76) Wang, R.; Gao, S.; Yang, Z.; Li, Y.; Chen, W.; Wu, B.; Wu, W. Engineered and Laser-Processed Chitosan Biopolymers for Sustainable and Biodegradable Triboelectric Power Generation. *Adv. Mater.* **2018**, *30*, No. 1706267.
(77) Kim, J.-N.; Lee, J.; Go, T. W.; Rajabi-Abhari, A.; Mahato, M.; Park, J. Y.; Lee, H.; Oh, I.-K. Skin-attachable and biofriendly chitosan-diatom triboelectric nanogenerator. *Nano Energy* **2020**, *75*, No. 104904.
(78) Choi, K.-H.; Park, S.; Hyeong, S.-K.; Bae, S.; Hong, J.-M.; Kim, T.-W.; Lee, S. H.; Ryu, S.; Lee, S.-K. Triboelectric effect of surface morphology controlled laser induced graphene. *J. Mater. Chem. A* **2020**, *8*, 19822−19832.

https://doi.org/10.1021/acsanm.3c01408
ACS Appl. Nano Mater. 2023, 6, 10453−10465